Radio constraints on dark matter annihilation in the galactic halo and its substructures

E. Borriello,[1,*] A. Cuoco,[2,†] and G. Miele[1,3,‡]

[1]*Dipartimento di Scienze Fisiche, Università "Federico II", Napoli, Italy & INFN Sezione di Napoli*

[2]*Department of Physics and Astronomy, University of Aarhus, Ny Munkegade, Bygn. 1520 8000 Aarhus Denmark*

[3]*Instituto de Física Corpuscular (CSIC-Universitat de València), Ed. Institutos de Investigación, Apartado de Correos 22085, E-46071 València, Spain*

(Received 26 September 2008; published 22 January 2009)

Annihilation of dark matter usually produces together with gamma rays comparable amounts of electrons and positrons. The e^+e^- gyrating in the galactic magnetic field then produce secondary synchrotron radiation which thus provides an indirect means to constrain the DM signal itself. To this purpose, we calculate the radio emission from the galactic halo as well as from its expected substructures and we then compare it with the measured diffuse radio background. We employ a multifrequency approach using data in the relevant frequency range 100 MHz–100 GHz, as well as the WMAP haze data at 23 GHz. The derived constraints are of the order $\langle \sigma_A v \rangle = 10^{-24}$ cm^3 s^{-1} for a DM mass $m_\chi =$ 100 GeV sensibly depending, however, on the astrophysical uncertainties, in particular, on the assumption of the galactic magnetic field model. The signal from single bright clumps is instead largely attenuated by diffusion effects and offers only poor detection perspectives.

DOI: 10.1103/PhysRevD.79.023518 PACS numbers: 95.35.+d, 95.85.Bh, 98.70.Vc

I. INTRODUCTION

Cosmology and astrophysics today provide compelling evidence of the existence of dark matter (DM) [1,2]. Nevertheless, its nature still remains elusive, and dark matter constituents have escaped a direct detection in the laboratory so far. Promising candidates are DM particles produced in thermal equilibrium in the early universe—the so-called weakly interacting massive particles (WIMPs). Theoretically, models of WIMPs naturally arise, for example, in supersymmetry (SUSY) as the lightest supersymmetric particle or as the lightest Kaluza-Klein particle in the framework of extra dimensions. These candidates are self-conjugates and can thus annihilate in couples to produce as final states neutrinos, photons, electrons, light nuclei (as wells as their antiparticles), etc., which can in principle be detected.

Among the indirect DM detection channels, gamma-ray emission represents one of the most promising opportunities due to the very low attenuation in the interstellar medium and to its high detection efficiency. See, for example, Refs. [2–4] for a review of this extensively studied issue. The expected neutrino detection rates are generally low although forthcoming km^3 detectors offer some promising prospects [5,6]. Finally, positrons and protons strongly interact with gas, radiation, and magnetic fields in the galaxy, and thus the expected signal sensibly depends on the assumed propagation model [7–9]. However, during the process of thermalization in the galactic medium, the high energy e^+ and e^- release secondary low energy radiation, in particular, in the radio and x-ray band, that, hence, can represent a chance to look for DM annihilation. Furthermore, while the astrophysical uncertainties affecting this signal are similar to the case of direct e^+, e^- detection, the sensitivities are quite different, and, in particular, the radio band allows for the discrimination of tiny signals even when the background is various orders of magnitudes more intense than the signal itself.

Indirect detection of DM annihilation through secondary photons has recently received increasing attention, exploring the expected signature in x-rays [10–12], at radio wavelengths [13–16], or both [17–19]. In the following we will focus our analysis on the radio signal expected from the Milky Way (MW) halo and its substructures. It is worth noticing that the halo signal has been recently discussed in Refs. [20–22] in connection with the Wilkinson Microwave Anisotropy Probe (WMAP) haze, which has been interpreted as a signal from DM annihilation. In this concern we will take in the following a more conservative approach by assuming that the current radio observations are entirely astrophysical in origin, and thus deriving constraints on the possible DM signal. The main point will be the use of further radio observations besides the WMAP ones, in the wide frequency range 100 MHz–100 GHz, and a comparison of the achievable bounds. Furthermore, the model dependence of these constraints on the assumed astrophysical inputs will be analyzed. We will also discuss the detection perspectives of the signal coming from the brightest DM substructures in the forthcoming radio surveys.

The paper is organized as follows. In Sec. II we will discuss the astrophysical inputs required to derive the DM signal such as the structure of the magnetic field, the DM spatial distribution, and the radio data employed to derive the constraints. In Sec. III we describe in detail the pro-

*eborriello@na.infn.it
†cuoco@phys.au.dk
‡miele@na.infn.it

cesses producing the DM radio signal either when it is originated from the halo or from the substructures. In Sec. IV we present and discuss our constraints, while in Sec. V we analyze the detection sensitivity to the signal coming from the single DM clump. In Sec. VI we give our conclusions and remarks.

II. ASTROPHYSICAL INPUTS

A. Dark matter distribution

Our knowledge of the DM spatial distribution on galactic and subgalactic scales has greatly improved thanks to recent high resolution zoomed N-body simulations [23–26]. These simulations indicate that for the radial profile of the galactic halo the usual Navarro-Frank-White (NFW) distribution [27]

$$\rho(r) = \frac{\rho_{\rm h}}{\frac{r}{r_{\rm h}}(1+\frac{r}{r_{\rm h}})^2} \tag{1}$$

still works as a good approximation over all the resolved scales. We will thus use this profile in the following. Note, anyway, that this choice is quite conservative with respect to other proposed profiles like the Moore profile [28], which exhibits an internal cusp $\propto r^{-1.5}$ that would give in principle a divergent DM annihilation signal from the center of the halo. Observationally, the situation is more uncertain. Baryons generally dominate the gravitational potential in the inner kpc's and fitting the data thus requires to model both the baryon and DM component at the same time. The NFW profile is in fair agreement with the observed Milky Way rotation curve [29], although, depending on the employed model, it is possible to find an agreement for many different DM profiles (see also [2] and references therein). We emphasize, however, that the various profiles differ mainly in the halo center (for $r \lesssim 1$ kpc) where the uncertainties, both in numerical simulations and from astrophysical observations are maximal. Thus, our analysis which explicitly excludes the galactic center, does not crucially depend on the choice of the profile.

A problem related to the profile of Eq. (1) is that the mass enclosed within the radius r is logarithmically divergent. A regularization procedure is thus required to define the halo mass. Following the usual conventions we define the mass of the halo as the mass contained within the *virial radius* $r_{\rm vir}$, defined as the radius within which the mean density of the halo is $\delta_{\rm vir} = 200$ times the mean *critical cosmological density* $\rho_{\rm cr}$ which, for a standard cosmological model ($\Omega_{\rm m} \simeq 0.3$, $\Omega_\Lambda \simeq 0.7$ [1]) is equal to $\rho_{\rm cr} \simeq 5 \times 10^{-6}$ GeV c^{-2} cm^{-3}. The parameters describing the halo are then determined imposing the DM density to be equal to $\rho_S = 0.365$ GeV c^{-2} cm^{-3} near the Solar System, at a galactocentric distance of $R_{\rm S} = 8.5$ kpc.

Simulations, however, predict a DM distribution sum of a smooth halo component, and of an additional clumpy one with total masses roughly of the same order of magnitude. Hereafter we will assume for the mass of the Milky Way $M_{\rm MW} = M_{\rm h} + M_{\rm cl} = 2 \times 10^{12} M_\odot$, where $M_{\rm h}$ and $M_{\rm cl}$ denote the total mass contained in the host galactic halo and in the substructures (subhaloes) distribution, respectively. The relative normalization is fixed by imposing that subhaloes in the range $10^7 M_\odot$, $10^{10} M_\odot$ have a total mass amounting to 10% of $M_{\rm MW}$ [23]. Current numerical simulations can resolve clumps with a minimum mass scale of $\sim 10^6 M_\odot$. However, for WIMP particles, clumps down to a mass of $10^{-6} M_\odot$ are expected [30,31]. We will thus consider a clump mass range between $10^{-6} M_\odot$ and $10^{10} M_\odot$.

Finally, to fully characterize the subhalo population we will assume a mass distribution $\propto m_{\rm cl}^{-2}$ and that they are spatially distributed following the NFW profile of the main halo. The mass spectrum number density of subhaloes, in galactocentric coordinates $\vec{r}$, is thus given by

$$\frac{dn_{\rm cl}}{dm_{\rm cl}}(m_{\rm cl}, \vec{r}) = A\left(\frac{m_{\rm cl}}{M_{\rm cl}}\right)^{-2}\left(\frac{r}{r_{\rm h}}\right)^{-1}\left(1+\frac{r}{r_{\rm h}}\right)^{-2}, \tag{2}$$

where A is a dimensional normalization constant. The above expression assumes some approximations: for example, a more realistic clump distribution should take into account tidal disruption of clumps near the galactic center. Numerical simulations suggest also that the radial distribution could be somewhat antibiased with respect to the host halo profile. However, with our conservative assumptions the DM annihilation signal is dominated by the host halo emission within up to 20°–30° from the galactic center so that the details of the subdominant signal from the clumps have just a slight influence on the final results. Recent results also show that mass distribution seems to converge to $m_{\rm cl}^{-1.9}$ rather than $m_{\rm cl}^{-2}$ [25]. This would also produce only a minor change in the following results.

Following the previous assumptions the total mass in DM clumps of mass between m_1 and m_2 results to be

$$\begin{aligned} M(m_1, m_2) &= \int d\vec{r} \int_{m_1}^{m_2} m_{\rm cl} \frac{dn_{\rm cl}}{dm_{\rm cl}}(m_{\rm cl}, \vec{r}) dm_{\rm cl} \\ &= 4\pi\left[\ln(1+c_{\rm h}) - \frac{c_{\rm h}}{1+c_{\rm h}}\right](A r_{\rm h}^3 M_{\rm cl}) \\ &\quad \times \ln\left(\frac{m_2}{m_1}\right) M_{\rm cl}, \end{aligned} \tag{3}$$

where $c_{\rm h} \equiv r_{\rm vir}/r_{\rm h}$ denotes the host halo concentration; while their number is

$$\begin{aligned} N(m_1, m_2) &= \int d\vec{r} \int_{m_1}^{m_2} \frac{dn_{\rm cl}}{dm_{\rm cl}}(m_{\rm cl}, \vec{r}) dm_{\rm cl} \\ &= 4\pi\left[\ln(1+c_{\rm h}) - \frac{c_{\rm h}}{1+c_{\rm h}}\right](A r_{\rm h}^3 M_{\rm cl}) \\ &\quad \times \left(\frac{M_{\rm cl}}{m_1} - \frac{M_{\rm cl}}{m_2}\right). \end{aligned} \tag{4}$$

Imposing the normalization condition $M(10^7 M_\odot, 10^{10} M_\odot) = 10\% M_{\rm MW}$, we finally get for the mass due to

the entire clumps distribution:

$$M_{\rm cl} = M(10^{-6}M_\odot, 10^{10}M_\odot) \sim 53.3\% M_{\rm MW}, \quad (5)$$

while for the number of these clumps we obtain

$$N(10^{-6}M_\odot, 10^{10}M_\odot) \sim 2.90 \times 10^{17}. \quad (6)$$

Finally by using the previous constraints one can fix the values of free parameters $r_{\rm h}$, $\rho_{\rm h}$, and A, hence obtaining $r_{\rm h} = 14.0$ kpc, that corresponds to a halo concentration of $c_{\rm h} = 14.4$, $\rho_{\rm h} = 0.572\ {\rm GeV\,c^{-2}\,cm^{-3}}$, and $A = 1.16 \times 10^{-19}\ {\rm kpc^{-3}} M_\odot^{-1}$.

A further piece of information is required to derive the annihilation signal from the clumps, namely, how the DM is distributed inside the clumps themselves. We will assume that each clump follows a NFW profile as the main halo with $r_{\rm cl}$ and $\rho_{\rm cl}$ replacing the corresponding quantities of Eq. (1). However, for a full characterization of a clump, further information on its concentration $c_{\rm cl}$ is required. Unluckily, numerical simulations are not completely helpful in this case, since we require information about the structure of clumps with masses down to $10^{-6}M_\odot$, far below the current numerical resolution. Analytical models are thus required. In the current cosmological scenario [1] structures formed hierarchically, *via* gravitational collapse, with smaller ones forming first. Thus, naively, since the smallest clumps formed when the Universe was denser, a reasonable expectation is $c_{\rm cl} \propto (1 + z_f)$, where z_f is the clump formation redshift. Following the model of Ref. [32] we will thus assume $c_{\rm cl} = c_1(\frac{m_{\rm cl}}{M_\odot})^{-\alpha}$ with $c_1 = 38.2$ and $\alpha = 0.0392$. With this concentration the integrated DM annihilation signal from all the substructures dominates over the smooth halo component only at about 30° from the galactic center (see Sec. III), so that the constraints on the DM signal do not crucially depend on the unresolved clumps signal, coming basically only from the smooth halo component. However, given the large uncertainties in the models, larger contributions from the unresolved population of clumps are in principle possible considering a different parametrization of the concentration (see, for example, the various models considered in [25,33]). We will not investigate further this possibility here. An enhancement of the clumps signal is also possible considering different choices of the clump profile other than the NFW: Differently from the case of the halo, in fact, the clump signal depends sensibly from the chosen profile and a Moore profile or an isothermal profile can in principle enhance the signal of several orders of magnitude. Also in this case we choose to quote conservative constraints and we will not consider these possibilities further.

B. Galactic magnetic field

The MW magnetic field is still quite uncertain especially near the galactic center. The overall structure is generally believed to follow the spiral pattern of the galaxy itself with a normalization of about $\sim 1\ \mu$G near the solar system. Eventually, a toroidal or a dipole component is considered in some model.

We will consider in the following the Tinyakov and Tkachev model (TT) [34] which is a fair representative of the available descriptions of the MW magnetic field. Within this model, the field shows the typical spiral pattern, an exponential decrease along the z axis and a $1/R$ behavior in the galactic plane. The field intensity in the inner kiloparsecs is constant at about 7 μG. We will use the slightly modified parametrization of this model as described in [35]. Higher normalizations are in principle possible considering more complex structures as, for example, a dipole or a toroidal component [36]. Indeed some recent analyses [37,38] including new available data seems to favor the presence of these further structures. We will thus consider as possible also a ''high normalization model'' that we simply parameterize as a constant 10 μG field. This choice is also motivated by a comparison with the results of [20,21] where the same magnetic field is used.

Further, beside the regular component, the galactic magnetic field presents a turbulent random component. The rms intensity of this component is generally expected of the same order of magnitude of the regular one, but both its spatial distribution and its spectrum are poorly known, thus here we neglect its effects. Naively, this random component is expected to affect the synchrotron maps that we will show in the following producing a blurring of the otherwise regular pattern. Also, the random component contributes to increase the overall normalization of the field. Thus without this component the synchrotron signal is slightly underestimated so that we can regard this choice as conservative.

C. Radio data

In the following we will derive constraints on the DM emission comparing the expected diffuse emission from the smooth halo and the unresolved population of clumps with all sky observation in the radio band. In the frequency range 100 MHz–100 GHz where the DM synchrotron signal is expected, various astrophysical processes contribute to the observed diffuse emission. Competing synchrotron emission is given by cosmic ray electrons accelerated in supernovae shocks dominating the radio sky up to $\sim$10 GHz. At higher frequencies the cosmic microwave background (CMB) and its anisotropies represent the main signal. However, thanks to the very sensitive multifrequency survey by the WMAP satellite, this signal (which represents thus a background for DM searches) can be modeled in a detailed way and can thus be removed from the observed radio galactic emission [39]. Other processes contributing in the 10–100 GHz range are given by thermal bremsstrahlung (free-free emission) of electrons on the galactic ionized gas and emission by small grains of vibrating or spinning dust.

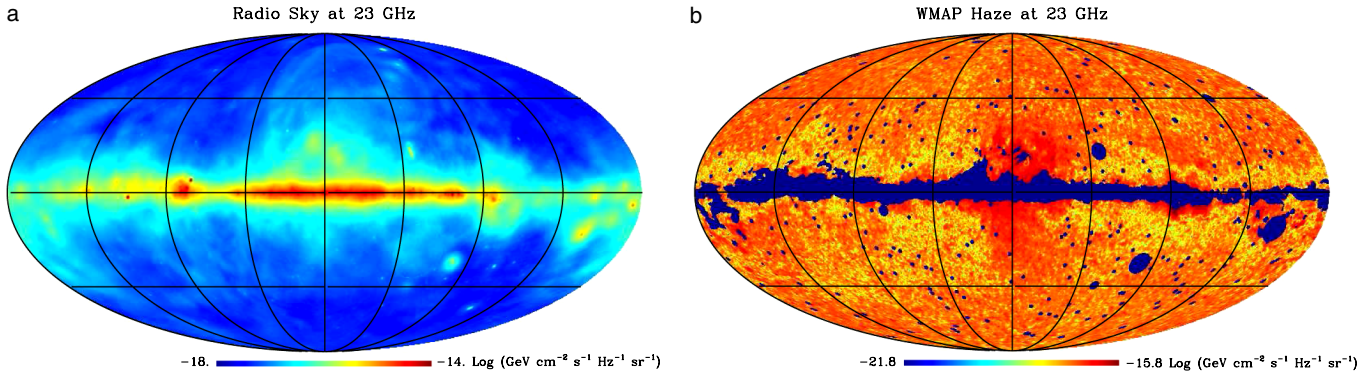

FIG. 1 (color online). Sky map of galactic foregrounds at the frequency of 23 GHz (left) and of the residual map showing the WMAP haze (right).

In the following our approach will be to compare the DM signal with the observed radio emission where only the CMB is modeled and removed. For this purpose we use the code described in [40] where most of the radio survey observations in the range 10 MHz–100 GHz are collected and a scheme to derive interpolated, CMB cleaned sky maps at any frequency in this range is described.

A more aggressive approach would be of course to try to model and subtract also the remaining emissions (synchrotron, free-free, dust) in order to compare the expected DM signal with the residual radio map. This is indeed the approach followed in [41,42] where residual maps at the five WMAP frequencies are derived using spatial templates for the various expected astrophysical components. The residual maps then exhibit the feature called the WMAP haze, which has been indeed interpreted as radio emission related to DM annihilation [20,43]. However, the fit procedure used for the haze extraction is crucial, and using more degrees of freedom to model the foregrounds as performed by the WMAP team [44] fails in finding the feature. We will anyway show in the following for comparison the constraints derived using the haze residual map at the WMAP frequency of 23 GHz [45]. A map of the haze and of the 1 GHz emission is shown in Fig. 1. We will see, however, that within our conservative approach, comparable or better constraints can be obtained thanks to the use of multifrequency information. For a given DM mass, in fact, 23 GHz is generally not the best frequency to use and better constraints are instead obtained using observations at lower frequencies even without further foreground modeling.

Definitely, a detailed foreground modeling at all radio frequencies would clearly give much stronger constraints on the DM signal and/or eventually confirm the DM nature of the WMAP haze. To this purpose consistent progress will be achieved in the next years with the new high quality data coming from the PLANCK mission and from low frequency arrays like Low Frequency Array (LOFAR) and Square Kilometer Array (SKA).

III. DM SYNCHROTRON SIGNAL

A. Particle physics

In a standard scenario where WIMPs experience a non-exotic thermal history, a typical mass range for these particles is 50 GeV $\lesssim m_\chi \lesssim$ 1 TeV, while a simple estimate for their (thermally averaged) annihilation cross section yields $\langle \sigma_A v \rangle = 3 \times 10^{-27}\ \mathrm{cm^3\ s^{-1}}/\Omega_{\mathrm{cdm}} h^2$ [3], giving $\langle \sigma_A v \rangle \approx 3 \times 10^{-26}\ \mathrm{cm^3\ s^{-1}}$ for $\Omega_{\mathrm{cdm}} h^2 \approx 0.1$ as resulting from the latest WMAP measurements [1]. However, this naive relation can fail badly if, for example, coannihilations play a role in the WIMP thermalization process [46], and a much wider range of cross sections should be considered viable. In this work we consider values of m_χ from about 10 GeV to about 1 TeV, and $\langle \sigma_A v \rangle$ in the range $(10^{-26} - 10^{-21})\ \mathrm{cm^3\ s^{-1}}$

The e^+e^- annihilation spectrum for a given supersymmetric WIMP candidate can be calculated, for example, with the DarkSUSY package [47]. However, the final spectrum has only a weak dependence on the exact annihilation process with the channels $\chi\chi \rightarrow ZZ, W^+W^-, q\bar{q}$ giving basically degenerate spectra. For leptonic channels like the $\tau^+\tau^-$ decaying mode, the spectrum differs significantly, although this channel has generally a quite low branching ratio. For simplicity we will assume hereafter full decay into the $q\bar{q}$ channel, hence e^- (e^+) will be emitted by decaying muons (antimuons) produced in pion decays. In this framework, the resulting e^+, e^- spectrum can be written as a convolution, namely,

$$\frac{dN_e}{dE_e}(E_e) = \int_{E_e}^{m_\chi c^2} dE_\mu \frac{dN_e^{(\mu)}}{dE_e}(E_e, E_\mu) \times \int_{E_\mu}^{E_\mu/\xi} dE_\pi W_\pi(E_\pi) \frac{dN_\mu^{(\pi)}}{dE_\mu}(E_\pi), \qquad (7)$$

with $\xi = (m_\mu/m_\pi)^2$, where

TABLE I. a_j values.

Coefficient	Analytical	Numerical
$a_{-3/2}$	$\frac{65}{189}\frac{1-\xi^{3/2}}{1-\xi}$	0.456
$a_{-1/2}$	$-\frac{66}{7}\frac{1}{1+\xi^{1/2}}$	−5.37
a_0	$\frac{25}{36}\frac{\xi^2-18\xi+8\xi^{1/2}+9}{(1-\xi)\xi^{1/2}}$	10.9
$a_{1/2}$	$9\frac{1-\xi^{-1/2}}{1-\xi}$	−6.77
a_2	$-\frac{3}{28}\frac{5\xi^2-42\xi+72\xi^{1/2}-35}{(1-\xi)\xi^{1/2}}$	0.969
a_3	$\frac{1}{189}\frac{35\xi^2-270\xi+424\xi^{1/2}-189}{(1-\xi)\xi^{1/2}}$	−0.185

$$\frac{dN_e^{(\mu)}}{dE_e}(E_e, E_\mu) = \frac{2}{E_\mu}\left[\frac{5}{6} - \frac{3}{2}\left(\frac{E_e}{E_\mu}\right)^2 + \frac{2}{3}\left(\frac{E_e}{E_\mu}\right)^3\right], \quad (8)$$

$$\frac{dN_\mu^{(\pi)}}{dE_\mu}(E_\pi) = \frac{1}{E_\pi}\frac{m_\pi^2}{m_\pi^2 - m_\mu^2}, \quad (9)$$

$$W_\pi(E_\pi) = \frac{1}{m_\chi c^2}\frac{15}{16}\left(\frac{m_\chi c^2}{E_\pi}\right)^{3/2}\left(1 - \frac{E_\pi}{m_\chi c^2}\right)^2. \quad (10)$$

In particular, Eq. (8) is the electron (positron) spectrum produced in the muon (antimuon) decay $\mu^- \to e^- \nu_\mu \bar{\nu}_e$ ($\mu^+ \to e^+ \bar{\nu}_\mu \nu_e$). Equation (9) stands for the μ^- (μ^+) spectrum from the $\pi^- \to \mu^- \bar{\nu}_\mu$ ($\pi^+ \to \mu^+ \nu_\mu$) decay process, and, finally, Eq. (10) provides a reasonable analytical approximation of the spectrum of pions from $q\bar{q}$ hadronization [48]. It is worth noticing that to achieve more accurate results Eq. (10) should be substituted by a numerical calculation, which, however, results not necessarily for the aim of the present paper as discussed in the following.

In this approximation the final electron (positron) spectrum can be cast in a simple polynomial form of the ratio $E_e/m_\chi c^2$:

$$\frac{dN_e}{dE_e}(E_e) = \frac{1}{m_\chi c^2}\sum_{j\in J} a_j \left(\frac{E_e}{m_\chi c^2}\right)^j, \quad (11)$$

where $J = \{-\frac{3}{2}, -\frac{1}{2}, 0, \frac{1}{2}, 2, 3\}$ and the coefficients a_j are listed in Table I.

The main advantage of using the above analytical approximation instead of a more accurate numerical input is that, as will be clear in the next section, most of the observables for the radio emission will be expressed in an analytical form as well. This, in turn, is of help for a better understanding of the physical results. Nevertheless, the difference with the complete numerical calculation turns out to be small, arising only for quite low electron energies, and thus for very low radio frequencies. At low energies, in fact, the analytical form has an asymptotic behavior $\propto E_e^{-1.5}$ while the numerical spectrum has a turn down. From a comparison with the numerical output from DarkSUSY for a 100 GeV WIMP with 100% branching ratio into $b\bar{b}$ the analytical form is a fair approximation until $E_e \approx 1$ GeV, which for a magnetic field $B \sim 10$ μG translates into a minimum valid frequency $\nu =$ 10–100 MHz, thus below the frequency window we are going to explore [see Eq. (20) below].

B. Electrons equilibrium distribution

Dark matter annihilation injects electrons in the galaxy at the constant rate

$$Q(E_e, r) = \frac{1}{2}\left(\frac{\rho(r)}{m_\chi}\right)^2 \langle\sigma_A v\rangle \frac{dN_e}{dE_e}. \quad (12)$$

On the other hand, the injected electrons lose energy interacting with the interstellar medium and diffuse away from the production site. In the limit in which convection and reacceleration phenomena can be neglected, the evolution of the e^+e^- fluid is described by the following diffusion-loss equation [49–51]

$$\frac{\partial}{\partial t}\frac{dn_e}{dE_e} = \vec{\nabla}\cdot\left[K(E_e, \vec{r})\vec{\nabla}\frac{dn_e}{dE_e}\right] + \frac{\partial}{\partial E_e}\left[b(E_e, \vec{r})\frac{dn_e}{dE_e}\right] + Q(E_e, \vec{r}), \quad (13)$$

where dn_e/dE_e stands for the number density of e^+, e^- per unit energy, $K(E_e, \vec{r})$ is the diffusion constant, and $b(E_e, \vec{r})$ represents the energy loss rate. The diffusion length of electrons is generally of the order of a kpc (see Sec. V) thus for the diffuse signal generated all over the galaxy, and thus over many kpc's, spatial diffusion can be neglected. This is not the case for the signal coming from a single clump for which the emitting region is much smaller than a kpc. We will further analyze this point in Sec. V. By neglecting diffusion, the steady state solution can be expressed as

$$\frac{dn_e}{dE_e}(E_e, \vec{r}) = \frac{\tau}{E_e}\int_{E_e}^{m_\chi c^2} dE_e' Q(E_e', \vec{r}), \quad (14)$$

where $\tau = E_e/b(E_e, \vec{r})$ is the cooling time, resulting from the sum of several energy loss processes that affect electrons. In the following we will consider synchrotron emission and inverse compton scattering (ICS) off the background photons (CMB and starlight) only, which are the faster processes and thus the ones really driving the electrons' equilibrium. Other processes, like synchrotron self absorption, ICS off the synchrotron photons, e^+e^- annihilation, Coulomb scattering over the galactic gas, and bremsstrahlung are generally slower. They can become relevant for an extremely intense magnetic field, possibly present in the inner parsecs of the galaxy [14], and thus will be neglected in this analysis.

For synchrotron emission the energy loss is given by (for example, see [52]) $b_{\rm syn}(E_e) = 4/3 c\sigma_T \gamma^2 \beta^2 U_B$ with $U_B = B^2/2\mu_0$ the magnetic energy density so that the time scale

of the energy loss is

$$\tau_{\rm syn} = \tau^0_{\rm syn}\left(\frac{B}{\mu{\rm G}}\right)^{-2}\left(\frac{E_e}{\rm GeV}\right)^{-1} \quad (15)$$

with $\tau^0_{\rm syn} = 3.95 \times 10^{17}$ s.

Similarly, for inverse compton emission the energy loss is given by $b_{\rm ICS}(E_e) = 4/3 c\sigma_{\rm T}\gamma^2\beta^2 U_{\rm rad}$. The relevant radiation background for ICS is given by an extragalactic uniform contribution consisting of the CMB with $U_{\rm CMB} = 8\pi^5(kT)^4/15(hc)^3 \approx 0.26$ eV/cm^3, the optical/infrared extragalactic background and the analogous spatially varying galactic contribution, the interstellar radiation field (ISRF). For the latter we use as a template the Galprop distribution model [53] which reduces to the extragalactic one at high galactocentric distances. In this model, the ISRF intensity near the solar position is about 5 eV/cm^3, and reaches values as large as 50 eV/cm^3 in the inner kpc's. With this model the ICS is always the dominant energy loss process, also near the galactic center (see Fig. 2). We thus have

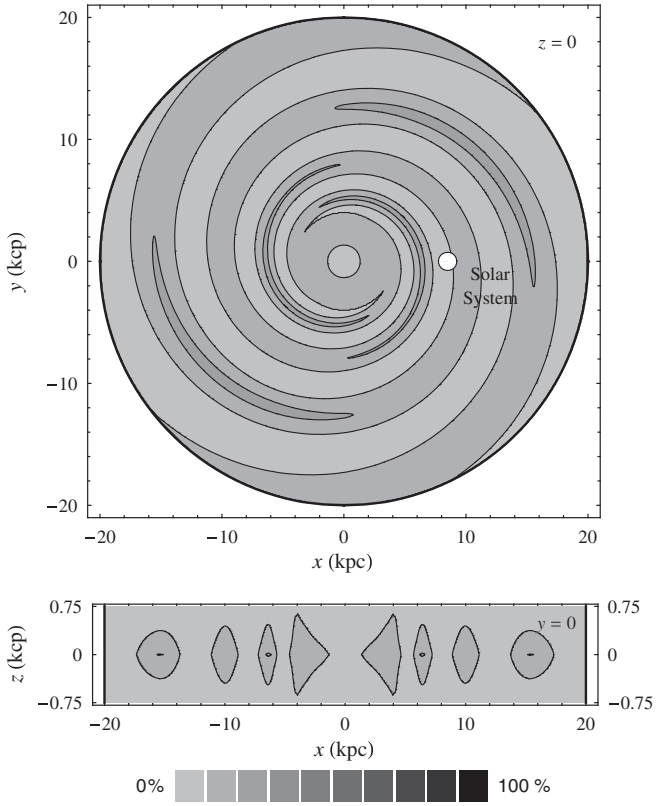

FIG. 2. Projections of the galaxy in the xy and xz planes showing the fractional synchrotron contribution to the e^+e^- total energy losses for TT model [34] of GMF and Galprop model [53] of ISRF. The synchrotron losses constitute generally no more than 20% of the total losses. The maximal percentage is reached at the center of the magnetic arms. In the remaining regions, included the galactic center, ICS is dominating.

$$\tau_{\rm ICS} = \tau^0_{\rm ICS}\left(\frac{U_{\rm rad}(\vec{r})}{\rm eV/cm^3}\right)^{-1}\left(\frac{E_e}{\rm GeV}\right)^{-1}, \quad (16)$$

with $\tau^0_{\rm ICS} = 9.82 \times 10^{15}$ s.

Finally, considering both the energy losses $b_{\rm tot} = b_{\rm syn} + b_{\rm ICS}$ we have

$$\tau(E_e, \vec{r}) = \left(\frac{E_e}{\rm GeV}\right)^{-1}\mu(\vec{r})\tau^0_{\rm syn}, \quad (17)$$

$$\mu(\vec{r}) = \left[\left(\frac{B(\vec{r})}{\mu{\rm G}}\right)^2 + \frac{\tau^0_{\rm syn}}{\tau^0_{\rm ICS}}\frac{U_{\rm rad}(\vec{r})}{\rm eV/cm^3}\right]^{-1}, \quad (18)$$

with the function $\mu(\vec{r})$ enclosing the whole spatial dependence.

By substituting the above expressions into Eq. (14) we get the following equilibrium distribution for electrons:

$$\frac{dn_e}{dE_e} = \frac{\langle\sigma_{\rm A}v\rangle\tau^0_{\rm syn}}{2m_\chi c^2}\mu(\vec{r})\left(\frac{\rho(r)}{m_\chi}\right)^2\sum_{k\in\mathcal{K}} b_k\left(\frac{m_\chi c^2}{\rm GeV}\right)^{-k} \times\left(\frac{E_e}{\rm GeV}\right)^{k-1}, \quad (19)$$

being $\mathcal{K} = J \cup \{-1\}$, $b_k = -a_k/(k+1)$, if $k \neq -1$, while $b_{-1} = \sum_{j\in J} a_j/(j+1)$.

C. Synchrotron spectrum

The synchrotron spectrum of an electron gyrating in a magnetic field has its prominent peak at the resonance frequency

$$\nu = \nu_0\left(\frac{B}{\mu{\rm G}}\right)\left(\frac{E_e}{\rm GeV}\right)^2, \quad (20)$$

with $\nu_0 = 3.7 \times 10^6$ Hz. This implies that, in practice, a δ approximation around the peaks works extremely well. Using this *frequency peak* approximation, the *synchrotron emissivity* can be defined as

$$j_\nu(\nu, \vec{r}) = \frac{dn_e}{dE_e}(E_e(\nu), \vec{r})\frac{dE_e(\nu)}{d\nu}b_{\rm syn}(E_e(\nu), \vec{r}). \quad (21)$$

This quantity is then integrated along the line of sight for the various cases to get the final synchrotron flux across the sky.

1. Single clump signal

According to the description in Sec. II A, let us consider a clump of mass $m_{\rm cl}$, whose center of mass is placed at $\vec{R}_{\rm cl}$ and with a sufficiently small size. In this case it is possible to neglect the spatial variation of $\mu(\vec{r})$ inside the clump itself, and thus the flux I_ν can be calculated as

$$I_\nu(\nu, \vec{R}_{\rm cl}) = \frac{1}{4\pi d^2_{\rm cl}}\int d\vec{r} j_\nu(\nu, \vec{R}_{\rm cl} + \vec{r}), \quad (22)$$

with $d_{\rm cl}$ the distance between the observer and the clump. This can be rewritten as

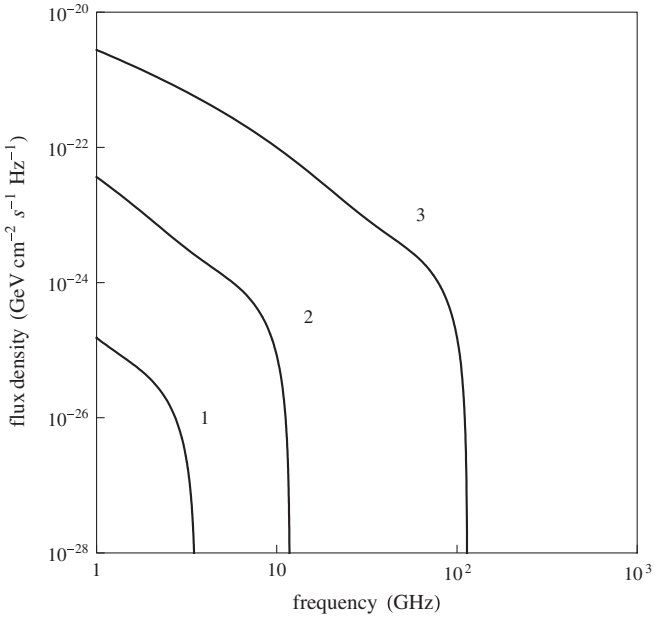

FIG. 3. Synchrotron flux density from three different clumps. The neutralino parameters are $m_\chi c^2 = 100$ GeV and $\langle \sigma_A v \rangle = 3 \times 10^{-26}$ cm^3 s^{-1}, while the relevant clump parameters are shown in Table II.

$$I_\nu(\nu, \vec{R}_{\rm cl}) = I^0_\nu \mu(\vec{R}_{\rm cl}) \sum_k A_k \left(\frac{B(\vec{R}_{\rm cl})}{\mu{\rm G}}\right)^{1-(k/2)} \left(\frac{\nu}{\rm Hz}\right)^{k/2}, \quad (23)$$

$$A_k(m_\chi) = b_k \left(\frac{m_\chi c^2}{\rm GeV}\right)^{-k} \left(\frac{\nu_0}{\rm Hz}\right)^{-(k/2)-1}, \quad (24)$$

with

$$\frac{I^0_\nu}{\rm GeV\,cm^{-2}\,s^{-1}\,Hz^{-1}} = 2.57 \times 10^{-12} \left(\frac{m_\chi c^2}{100\ {\rm GeV}}\right)^{-3} \times \frac{\langle \sigma_A v \rangle}{10^{-26}\ {\rm cm^3\,s^{-1}}} \left(\frac{r_{\rm cl}}{\rm kpc}\right)^3 \left(\frac{d_{\rm cl}}{\rm kpc}\right)^{-2} \times \left(\frac{\rho_{\rm cl}}{\rm GeV\,c^{-2}\,cm^{-3}}\right)^2. \quad (25)$$

Figure 3 shows some examples of signal, produced by three clumps of our simulation. An important feature to notice is that the synchrotron signal sensibly depends on the magnetic field both in the normalization and in the covered frequency range. In particular, the signal frequency cutoff, remnant of the energy spectrum cutoff near m_χ, depends on B following Eq. (20).

Figure 4 shows instead the positions and radio intensities for a realization of the clumps distribution with masses $m_{\rm cl} > 10^7 M_\odot$. It can be seen that all the clumps with a nonnegligible signal lie near the galactic plane where most of the galactic magnetic field is concentrated. Few clumps are visible at high latitude just because of projection effects, being located very near and slightly up or below the solar position with respect to the galactic plane.

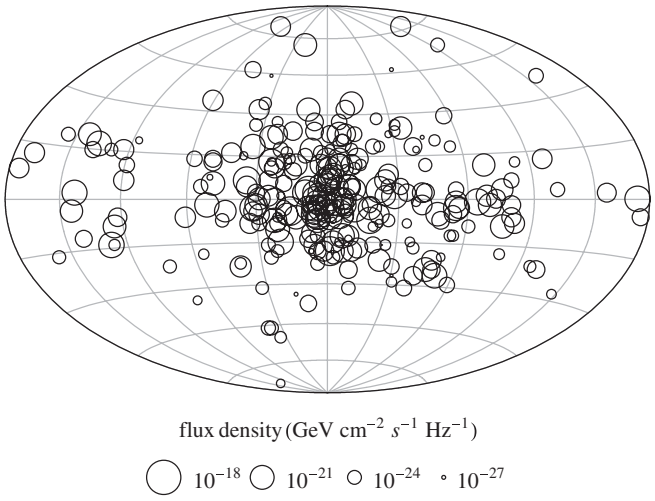

FIG. 4. Sky map at the frequency of 1 GHz for a realization of clumps distribution. For each clump, the circle radius is proportional to the logarithm of radio flux.

2. Diffuse signals

The diffuse halo signal is similarly given by the integral along the line of sight of Eq. (21)

$$\frac{d^2 I_\nu}{dl db} = \frac{\cos b}{4\pi} \int_0^\infty j_\nu ds, \quad (26)$$

where (l, b) are coordinates on the sphere and s the line of sight coordinate. To calculate the total contribution from the substructures, instead, we have to sum over all haloes

$$\frac{d^2 I^{\rm unr}_\nu}{dl db} = \cos b \int dm_{\rm cl} \int ds s^2 \frac{dn_{\rm cl}}{dm_{\rm cl}}(m_{\rm cl}, \vec{r}) I^{\rm res}_\nu(\nu, \vec{r}), \quad (27)$$

with $I^{\rm res}_\nu$ given by Eq. (23) and $\vec{r} = \vec{r}(s, l, b)$.

Interestingly, the sum of the two diffuse contributions can be rewritten as

$$\frac{d^2 I^{\rm DM}_\nu}{dl db} = \frac{\cos b}{4\pi} \int j^{\rm DM}_\nu ds, \quad (28)$$

where

$$j^{\rm DM}_\nu = \frac{1}{4} \left(\frac{m_\chi c^2}{\rm GeV}\right)^{-3} \frac{\langle \sigma_A v \rangle}{\rm cm^3\,s^{-1}} \left\{ \left[\frac{\rho_{\rm h}/{\rm GeV\,c^{-2}\,cm^{-3}}}{(r/r_{\rm h})(1 + r/r_{\rm h})^2} \right]^2 + \frac{\rho_{\rm CL}/{\rm GeV\,c^{-2}\,cm^{-3}}}{(r/r_{\rm h})(1 + r/r_{\rm h})^2} \right\} \mu(\vec{r}) \sum_k A_k(m_\chi) \left(\frac{B(\vec{r})}{\mu{\rm G}}\right)^{1-k/2} \times \left(\frac{\nu}{\rm Hz}\right)^{k/2} {\rm GeV\,cm^{-3}\,s^{-1}\,Hz^{-1}\,sr^{-1}}. \quad (29)$$

Thus, from the point of view of DM annihilation the unresolved clumps signal behaves like a further smooth NFW component with the same scale radius of the halo profile, but with a different *effective density* $\rho_{\rm CL} = 0.604$ GeV c^{-2} cm^{-3}, and with an emissivity simply proportional to the density profile instead of its square.

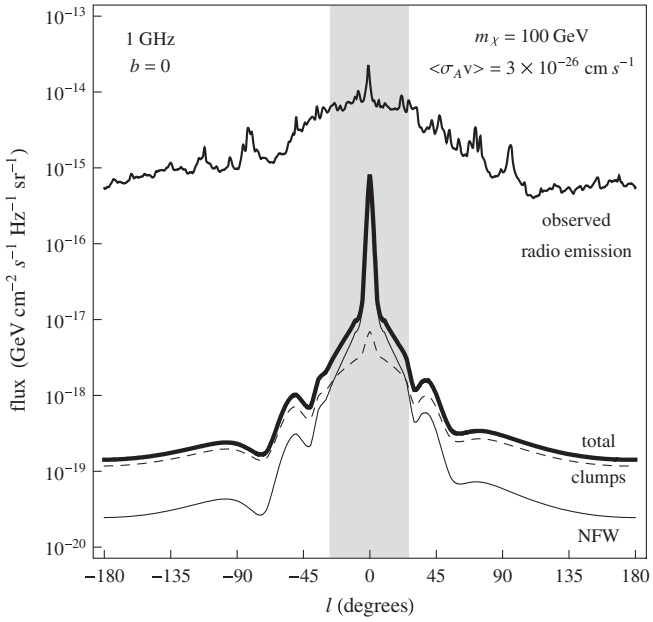

FIG. 5. DM synchrotron profile for the halo and unresolved substructures and their sum at 1 GHz for $m_\chi = 100$ GeV and $\langle\sigma_A v\rangle = 3 \times 10^{-26}$ cm^3 s^{-1}. The astrophysical observed emission at the same frequency is also shown. The gray band indicates the angular region within which the DM signal from the host halo dominates over the signal from substructures modeled as in Sec. II A.

We see that the halo component dominates in the central region of the galaxy, where

$$\frac{r}{r_h}\left(1+\frac{r}{r_h}\right)^2 < \frac{\rho_h^2}{\rho_{CL}} \Rightarrow r < 4.39 \text{ kpc} \qquad (30)$$

which corresponds to a disk of radius 27.3 degrees (see Fig. 5).

IV. DM ANNIHILATION CONSTRAINTS

The pattern and intensity of the DM radio map resulting from the sum of the contributions from the smooth halo and unresolved clumps is shown in Fig. 6 for $m_\chi = 100$ GeV and $\langle\sigma_A v\rangle = 3 \times 10^{-26}$ cm^3 s^{-1}. Similar maps are obtained at different frequencies and different m_χ and $\langle\sigma_A v\rangle$ to obtain DM exclusion plots. For our analysis we use a small mask covering a $15° \times 15°$ region around the galactic center where energy loss processes other than synchrotron and ICS start possibly to be relevant. We include the galactic plane although this region has basically no influence for the constraints on the DM signal.

In Fig. 7 we show the radio constraints on the DM annihilation signal in the $m_\chi - \langle\sigma_A v\rangle$ plane for various frequencies and various choices of the foreground. Several comments are in order. First, we can see that, as expected, the use of the haze at 23 GHz gives about 1 order of magnitude better constraints with respect to the synchrotron foregrounds at the same frequency. However, using also the information at other frequencies almost the same constraints can be achieved. This information, in particular, is complementary giving better constraints at lower DM masses. This is easily understood since a smaller DM mass increases the annihilation signal ($\propto m_\chi^{-2}$) at smaller energies, and thus smaller synchrotron frequencies. In particular, the constraints improve of about 1 order of magnitude at $m_\chi \sim 100$ GeV from 23 GHz to 1 GHz while only a modest improvement is achieved considering further lower frequencies as 0.1 GHz. This saturation of the constraints is due to the frequency dependence of the DM signal, that below 1 GHz becomes flatter than the astrophysical backgrounds so that the fraction of contribution from DM is maximal at about 1 GHz. Further, the constraints show a threshold behavior given basically by Eq. (20) which settles a maximum emitted radio frequency for a given DM mass m_χ. This threshold behavior is, for example, clearly seen at 23 GHz in the right panel of Fig. 7 where only for masses above ~40 GeV the cross section is constrained.

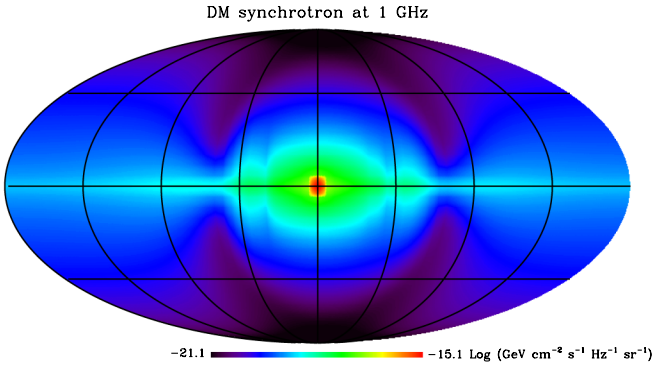

FIG. 6 (color online). Sky map of the galactic radio signal generated by the DM smooth halo and unresolved clumps at the frequency of 1 GHz for $m_\chi = 100$ GeV and $\langle\sigma_A v\rangle = 3 \times 10^{-26}$ cm^3 s^{-1}. The peculiar shape of the signal, pinched approximately at $\pm 30°$ and $\pm 60°$, reflects basically the structure of the magnetic field as seen in projection from the Solar System, where the observer is located (compare also with Fig. 2). The galactic center region and the first few magnetic arms are visible as regions of high magnetic field intensity and hence prominent synchrotron emission.

Notice that although the astrophysical background which we compare with at 1 GHz is an interpolation, the derived constraints are still valid given the smooth behavior and the broad frequency extent of the DM signal, which does not exhibit narrow peaks at particular frequencies. However, effective measurements have been performed, for example, at 408 MHz and 1.4 GHz (see [40]). Quoting our constraints at these exact frequencies would change the results only slightly.

The DM signal has thus a broad frequency extent and also below 1 GHz is still relevant. This is a potential problem for the DM interpretation of the WMAP haze

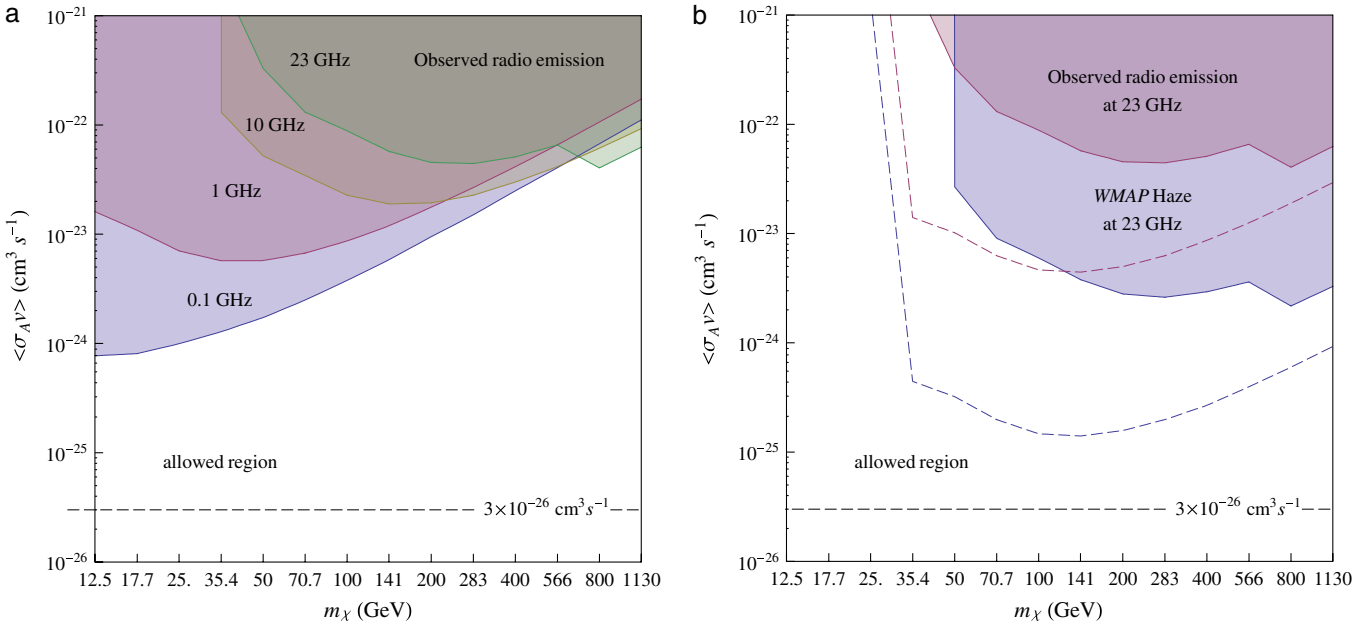

FIG. 7 (color online). Left: constraints in the $m_\chi - \langle\sigma_A v\rangle$ plane for various frequencies without assuming synchrotron foreground removal. Right: Constraints from the WMAP 23 GHz foreground map and 23 GHz foreground-cleaned residual map (the WMAP haze) for the TT model of magnetic field (filled regions) and for a uniform 10 μG field (dashed lines).

given that, in the haze extraction procedure, the observed radio emission at 408 MHz is used as template of the synchrotron background. In fact, naively, a DM signal at 23 GHz should be relevant at 408 MHz as well, unless either the DM mass or the magnetic field is so high to shift the DM contribution to higher frequencies and making it negligible at 408 MHz.

The second relevant point to notice is that the constraint depends quite sensibly on the magnetic field assumptions. The constraints we obtain with the TT model are generally almost 2 orders of magnitude weaker with respect to the results reported in [21]. They are instead more in agreement with [22] where Galprop has been employed to calculate the DM synchrotron signal. For a closer comparison with [21] we choose, as they do, a constant magnetic field of 10 μG although still keeping the Galprop ISRF model. Even in this case our derived constraints are a factor of 5 weaker (despite the inclusion of the contribution from substructures). The remaining factor of 5 can be finally recovered using a constant ISRF with $U_{\rm rad} = 5$ eV/cm^3 as assumed in [21]. In this case, in fact, the smaller values of $U_{\rm rad}$ reduces the ICS losses enhancing in turn the synchrotron signal. It should be said, however, that while the magnetic field normalization is still quite uncertain, the ISRF is instead more constrained and a large variation with respect to the Galprop model seems unlikely.

The constraints shown in Fig. 7 extend down to $\sim$10 GeV, which is somewhat the mass limit for a conservative analysis. It is clear that for low masses the constraints come more and more from lower frequencies. For example for a WIMP of 30 GeV the data at 100 MHz are 2 orders of magnitude more constraining than the data at 10 GHz. However, extremely low frequencies are not experimentally accessible. For a WIMP of 1 GeV, from Eq. (20) with a magnetic field of $\mathcal{O}(\mu$G) only frequencies $\lesssim$ 10 MHz would be useful to place constraints on the DM signal. Although observations at this frequency exist [40], in general the survey sky coverage is quite incomplete and the data quality is nonoptimal. Observations in this very low frequency range should substantially improve with the next generation radio arrays LOFAR and SKA. WIMP masses below 1 GeV still would produce observable synchrotron radiation at the galactic center where the magnetic field is likely much higher than the μG scale [possibly $\mathcal{O}(m$G)]. This kind of analysis, however, would be quite model dependent and would face further background uncertainties.

V. SINGLE CLUMPS DETECTABILITY

To have a reliable estimate of the sensitivity to a single clump detection, diffusion effects cannot be neglected. Although the integrated synchrotron clump signal is given by Eq. (23), the clumps appear extended rather than point-like with a dimension typically of several degrees. As a reasonable approximation we can assume that the signal is spread over an area of radius equal to the diffusion length of the electrons $l_D = \sqrt{K(E_e)\tau_{\rm loss}(E_e)}$, where K is the diffusion coefficient and $\tau_{\rm loss}$ is the energy loss time given by Eq. (17). We use for K the Galprop model [49]

TABLE II. Parameters of the example clumps chosen in Fig. 3.

Clump	$d_{\rm cl}$	$r_{\rm cl}$	$\rho_{\rm cl}$	B	Flux density at 1 GHz
#	kpc	kpc	GeV c^{-2} cm^{-3}	μG	GeV cm^{-2} s^{-1} Hz^{-1}
1	14.2	0.180	6.51	0.0962	1.70×10^{-25}
2	4.71	0.181	6.50	0.320	4.55×10^{-23}
3	5.50	0.188	6.404	3.08	2.66×10^{-21}

$$K = K_0 \left(\frac{E_e}{E_{e0}}\right)^{\delta}, \tag{31}$$

with a reference energy $E_{e0} = 3$ GeV, a Kolmogorov spectrum $\delta = 1/3$, and $K_0 = 10^{28}$ cm^2/s.

Taking as reference the parameters of a very bright clump like the #3 in Table II, we get (1 pc $= 3 \times 10^{18}$ cm)

$$l_D = \sqrt{K(E_e)\left(\frac{E_e}{\rm GeV}\right)^{-1} \mu(\vec{x})\tau^0_{\rm syn}} \approx 1 \text{ kpc}, \tag{32}$$

for $E_e \approx 10$ GeV and for a radiation density $U_{\rm rad} \approx 5$ eV/cm^3. The energy losses are basically dominated by ICS thus the result is almost independent of the magnetic field value. Moreover the dependence on the electron energy and the radiation density itself is very weak. Of course the clumps will have a certain profile peaked in the center and will not be perfectly smoothed all over l_D. However, the dilution of the signal in the much larger volume with respect to the region of emission makes it quite hard to detect the clump. We can consider, for example, the signal from a very bright clump at a distance of 5 kpc with a flux of 10^{-22} GeV cm^{-2} s^{-1} Hz^{-1} at 20 GHz, corresponding approximately to the characteristics of clump #3 in Fig. 3. With a dilution over 1 kpc, the clump emission is seen under a steradian $A = \pi\alpha^2 \approx 0.1$ sr with $\alpha \approx 10°$, giving a diffuse clump flux of 10^{-21} GeV cm^{-2} s^{-1} Hz^{-1} sr^{-1}. The WMAP sensitivity of about 10 μK translates into a flux sensitivity[1] of $\sim 10^{-18}$ GeV cm^{-2} s^{-1} Hz^{-1} sr^{-1}, meaning that the expected, optimistic signal is about 3 orders of magnitude below the reach of the current sensitivity. The situation is only slightly better at 150 MHz where the expected LOFAR sensitivity is 50 mK [54] i.e. $\sim 2 \times 10^{-19}$ GeV cm^{-2} s^{-1} Hz^{-1} sr^{-1}.

The chance of clump radio detection seems thus quite poor even with the next generation experiments. On the other side, the fact that the signal is anyway extended and not pointlike makes the clump signal not really complementary to the diffuse component sharing the same systematics with a much fainter signal. It is likely thus that the a role for DM investigations in the radio will be played basically by the diffuse signal.

[1]At radio frequencies the Rayleigh-Jeans law $F_\nu = 2\nu^2/c^2 k_{\rm B} T$ is employed to translate fluxes into brightness temperatures.

VI. SUMMARY AND CONCLUSIONS

Using conservative assumptions for the DM distribution in our galaxy we derive the expected secondary radiation due to synchrotron emission from high energy electrons produced in DM annihilation. The signal from single bright clumps offers only poor sensitivities because of diffusion effects which spread the electrons over large areas diluting the radio signal. The diffuse signal from the halo and the unresolved clumps is instead relevant and can be compared to the radio astrophysical background to derive constraints on the DM mass and annihilation cross section.

Constraints in the radio band, in particular, are complementary to similar (less stringent but less model dependent) constraints in the x-ray/gamma band [55,56] and from neutrinos [57]. Radio data, in particular, are more sensitive in the GeV–TeV region while neutrinos provide more stringent bounds for very high DM masses ($\gtrsim 10$ TeV). Gammas, instead, are more constraining for $m_\chi \lesssim 1$ GeV. The combination of the various observations provides thus interesting constraints over a wide range of masses pushing the allowed window significantly near the thermal relic possibility.

More into details, we obtain conservative constraints at the level of $\langle\sigma_{\rm A} v\rangle \sim 10^{-23}$ cm^3 s^{-1} for a DM mass $m_\chi = 100$ GeV from the WMAP haze at 23 GHz. However, depending on the astrophysical uncertainties, in particular, on the assumption on the galactic magnetic field model, constraints as strong as $\langle\sigma_{\rm A} v\rangle \sim 10^{-25}$ cm^3 s^{-1} can be achieved. Complementary to other works which employ the WMAP haze at 23 GHz, we also use the information in a wide frequency band in the range 100 MHz–100 GHz. Adding this information the constraints become of the order of $\langle\sigma_{\rm A} v\rangle \sim 10^{-24}$ cm^3 s^{-1} for a DM mass $m_\chi = 100$ GeV. The multifrequency approach thus gives comparable constraints with respect to the WMAP haze only, or generally better for $m_\chi \lesssim 100$ GeV where the best sensitivity is achieved at $\sim$ GHz frequencies.

The derived constraints are quite conservative because no attempt to model the astrophysical background is made differently from the case of the WMAP haze. Indeed, the haze residual map itself should be interpreted with some caution, given that the significance of the feature is at the moment still debated and complementary analyses from different groups (as the WMAP one) miss in finding a clear evidence of the feature. In this respect, the multifrequency

approach will be definitely necessary to clarify the nature of controversial DM signals as in the case of the WMAP haze. Progresses are expected with the forthcoming data at high frequencies from Planck and at low frequencies from LOFAR and, in a more distant future, from SKA. These surveys will help in disentangling the various astrophysical contributions thus assessing the real significance of the Haze feature. Further, the low frequency data, in particular, will help to improve our knowledge of the galactic magnetic field. Progresses in these fields will provide a major improvement for the interpretation of the DM radio connection.

ACKNOWLEDGMENTS

We wish to thank P. D. Serpico for valuable comments and T. Di Girolamo for a careful reading of the draft. Use of the publicly available HEALPix software [58] is acknowledged. G. M. acknowledges supports by the Spanish MICINN (Grants No. SAB2006-0171 and No. FPA2005-01269) and by INFN-I.S.Fa51 and PRIN 2006 "Fisica Astroparticellare: Neutrini ed Universo Primordiale" of Italian MIUR.

[1] E. Komatsu *et al.* (WMAP Collaboration), arXiv:0803.0547.
[2] G. Bertone, D. Hooper, and J. Silk, Phys. Rep. **405**, 279 (2005).
[3] G. Jungman, M. Kamionkowski, and K. Griest, Phys. Rep. **267**, 195 (1996).
[4] L. Bergstrom, Rep. Prog. Phys. **63**, 793 (2000).
[5] L. Bergstrom, J. Edsjo, and P. Gondolo, Phys. Rev. D **58**, 103519 (1998).
[6] V. D. Barger, F. Halzen, D. Hooper, and C. Kao, Phys. Rev. D **65**, 075022 (2002).
[7] E. A. Baltz and J. Edsjo, Phys. Rev. D **59**, 023511 (1998).
[8] D. Hooper and J. Silk, Phys. Rev. D **71**, 083503 (2005).
[9] F. Donato, N. Fornengo, D. Maurin, and P. Salati, Phys. Rev. D **69**, 063501 (2004).
[10] L. Bergstrom, M. Fairbairn, and L. Pieri, Phys. Rev. D **74**, 123515 (2006).
[11] M. Regis and P. Ullio, Phys. Rev. D **78**, 043505 (2008).
[12] T. E. Jeltema and S. Profumo, arXiv:0805.1054.
[13] P. Blasi, A. V. Olinto, and C. Tyler, Astropart. Phys. **18**, 649 (2003).
[14] R. Aloisio, P. Blasi, and A. V. Olinto, J. Cosmol. Astropart. Phys. 05 (2004) 007.
[15] A. Tasitsiomi, J. M. Siegal-Gaskins, and A. V. Olinto, Astropart. Phys. **21**, 637 (2004).
[16] L. Zhang and G. Sigl, J. Cosmol. Astropart. Phys. 09 (2008) 027.
[17] S. Colafrancesco, S. Profumo, and P. Ullio, Astron. Astrophys. **455**, 21 (2006).
[18] S. Colafrancesco, S. Profumo, and P. Ullio, Phys. Rev. D **75**, 023513 (2007).
[19] E. A. Baltz and L. Wai, Phys. Rev. D **70**, 023512 (2004).
[20] D. Hooper, D. P. Finkbeiner, and G. Dobler, Phys. Rev. D **76**, 083012 (2007).
[21] D. Hooper, Phys. Rev. D **77**, 123523 (2008).
[22] P. Grajek, G. Kane, D. J. Phalen, A. Pierce, and S. Watson, arXiv:0807.1508.
[23] J. Diemand, B. Moore, and J. Stadel, Nature (London) **433**, 389 (2005).
[24] J. Diemand, M. Kuhlen, and P. Madau, Astrophys. J. **657**, 262 (2007).
[25] M. Kuhlen, J. Diemand, and P. Madau, arXiv:0805.4416.
[26] V. Springel *et al.*, arXiv:0809.0898.
[27] J. F. Navarro, C. S. Frenk, and S. D. M. White, Astrophys. J. **490**, 493 (1997).
[28] B. Moore, S. Ghigna, F. Governato, G. Lake, T. R. Quinn, J. Stadel, and P. Tozzi, Astrophys. J. **524**, L19 (1999).
[29] A. Klypin, H. Zhao, and R. S. Somerville, Astrophys. J. **573**, 597 (2002).
[30] S. Hofmann, D. J. Schwarz, and H. Stoecker, Phys. Rev. D **64**, 083507 (2001).
[31] A. M. Green, S. Hofmann, and D. J. Schwarz, J. Cosmol. Astropart. Phys. 08 (2005) 003.
[32] J. S. Bullock *et al.*, Mon. Not. R. Astron. Soc. **321**, 559 (2001).
[33] L. Pieri, G. Bertone, and E. Branchini, Mon. Not. R. Astron. Soc. **384**, 1627 (2008).
[34] P. G. Tinyakov and I. I. Tkachev, Astropart. Phys. **18**, 165 (2002).
[35] M. Kachelriess, P. D. Serpico, and M. Teshima, Astropart. Phys. **26**, 378 (2007).
[36] M. Prouza and R. Smida, Astron. Astrophys. **410**, 1 (2003).
[37] X. H. Sun, W. Reich, A. Waelkens, and T. Ensslin, Astron. Astrophys. **477**, 573 (2008).
[38] A. Noutsos, S. Johnston, M. Kramer, and A. Karastergiou, Mon. Not. R. Astron. Soc. **386**, 1881 (2008).
[39] M. Tegmark, A. de Oliveira-Costa, and A. Hamilton, Phys. Rev. D **68**, 123523 (2003).
[40] A. de Oliveira-Costa, M. Tegmark, B. M. Gaensler, J. Jonas, T. L. Landecker, and P. Reich, arXiv:0802.1525.
[41] D. P. Finkbeiner, Astrophys. J. **614**, 186 (2004).
[42] G. Dobler and D. P. Finkbeiner, Astrophys. J. **680**, 1222 (2008).
[43] D. P. Finkbeiner, arXiv:astro-ph/0409027.
[44] B. Gold *et al.* (WMAP Collaboration), arXiv:0803.0715.
[45] The map of the haze at 23 GHz can be downloaded from http://www.skymaps.info/.
[46] K. Griest and D. Seckel, Phys. Rev. D **43**, 3191 (1991).
[47] P. Gondolo, J. Edsjo, P. Ullio, L. Bergstrom, M. Schelke, and E. A. Baltz, J. Cosmol. Astropart. Phys. 07 (2004) 008.
[48] C. T. Hill, Nucl. Phys. **B224**, 469 (1983).
[49] I. V. Moskalenko and A. W. Strong, Astrophys. J. **493**, 694 (1998).

[50] A. W. Strong and I. V. Moskalenko, Astrophys. J. **509**, 212 (1998).
[51] A. W. Strong, I. V. Moskalenko, and O. Reimer, Astrophys. J. **537**, 763 (2000); **541**, 1109(E) (2000).
[52] M. S. Longair, *High Energy Astrophysics* (Cambridge University Press, Cambridge, England, 1982), 2nd ed.
[53] T. A. Porter and A. W. Strong, arXiv:astro-ph/0507119.
[54] V. Jelic *et al.*, arXiv:0804.1130.
[55] G. D. Mack, T. D. Jacques, J. F. Beacom, N. F. Bell, and H. Yuksel, Phys. Rev. D **78**, 063542 (2008).
[56] M. Kachelriess and P. D. Serpico, Phys. Rev. D **76**, 063516 (2007).
[57] H. Yuksel, S. Horiuchi, J. F. Beacom, and S. Ando, Phys. Rev. D **76**, 123506 (2007).
[58] K. M. Gorski, E. Hivon, A. J. Banday, B. D. Wandelt, F. K. Hansen, M. Reinecke, and M. Bartelman, Astrophys. J. **622**, 759 (2005).